symmetry

MDPI

Case Report

Influence of Wind Speed, Wind Direction and Turbulence Model for Bridge Hanger: A Case Study

Yang Ding [1], Shuang-Xi Zhou [2], Yong-Qi Wei [3], Tong-Lin Yang [4] and Jing-Liang Dong [2,*]

1 Department of Civil Engineering, Zhejiang University, Hangzhou 310058, China; ceyangding@zju.edu.cn
2 School of Civil Engineering and Architecture, East China Jiaotong University, Nanchang 330013, China; green.55@163.com
3 School of Materials Science and Engineering, Tongji University, Shanghai 201804, China; wei_yongqi@tongji.edu.cn
4 College of Chemistry and Chemical Engineering, Hunan University, Changsha 410082, China; ytl181431@hnu.edu.cn
* Correspondence: 13677089341@163.com

Abstract: Wind field (e.g., wind speed and wind direction) has the characteristics of randomness, nonlinearity, and uncertainty, which can be critical and even destructive on a long-span bridge's hangers, such as vortex shedding, galloping, and flutter. Nowadays, the finite element method is widely used for model calculation, such as in long-span bridges and high-rise buildings. In this study, the investigated bridge hanger model was established by COMSOL Multiphysics software, which can calculate fluid dynamics (CFD), solid mechanics, and fluid–solid coupling. Regarding the wind field of bridge hangers, the influence of CFD models, wind speed, and wind direction are investigated. Specifically, the bridge hanger structure has symmetrical characteristics, which can greatly reduce the calculation efficiency. Furthermore, the von Mises stress of bridge hangers is calculated based on fluid–solid coupling.

Keywords: wind field characteristics; finite element model; fluid–solid coupling; long-span bridge hangers

Citation: Ding, Y.; Zhou, S.-X.; Wei, Y.-Q.; Yang, T.-L.; Dong, J.-L. Influence of Wind Speed, Wind Direction and Turbulence Model for Bridge Hanger: A Case Study. *Symmetry* **2021**, *13*, 1633. https://doi.org/10.3390/sym13091633

Academic Editor: Marco Montemurro

Received: 2 August 2021
Accepted: 2 September 2021
Published: 5 September 2021

1. Introduction

In recent years, the structure of long-span bridges has been softer, and their crossing ability has shown a continuous increase due to the advance in design and construction technologies and the emergence of novel materials [1]. However, a long-span bridge does not work properly and is even destroyed under wind effects, which include vortex shedding, galloping, flutter, and so forth [2]. For example, vortex-induced vibrations may result in long-term fatigue damage, shortening the bridge life [3]. Galloping can lead to significant amplitude oscillation of the bridge [4]. Long-span bridges may be affected by dynamic instability phenomena, that is, flutter [5]. Therefore, it is important to analyze the impact of long-span bridges under wind fields (e.g., wind speed and wind direction), which can ensure a reliable wind-resistant design of a bridge [6–12].

In order to study the impact of long-span bridges under wind fields (e.g., wind speed and wind direction), computational fluid dynamics [13–17] has been proposed based on structural health monitoring (SHM) data. Regarding the influence of wind direction, Zhu et al. (2012) [18] found variations of aerodynamic coefficients with wind direction based on the results of wind tunnel tests. However, wind tunnel tests cannot be widely used in the study of a wind-induced structural response because these tests require a substantial amount of resources, where these tests are limited to a certain number of pressure taps, and some information about separation zones, recirculation, and so forth might get lost [19,20]. On the contrary, the numerical calculation method, that is, computational fluid dynamics model, can obtain the corresponding structural stress response by setting different wind speeds and wind directions based on the finite element method [21]. For example, Huang et al. [22] ran a 3D CFD model to examine scale effects on turbulent flow

and sediment scour. Shirai et al. [23] studied the applicability of the two-dimensional Reynolds-averaged numerical simulation for predicting the flow around a self-oscillating bridge deck section. Thus, the computational fluid dynamics model allows for an accurate evaluation of the impact of long-span bridges under wind fields since it directly utilizes SHM data.

The main contributions of this work are threefold: (1) The bridge hanger model was established by COMSOL Multiphysics software, which can calculate computational fluid dynamics. (2) Regarding the bridge hanger, the influence of wind speed, wind direction, and turbulence model was investigated. The rest of the paper is organized as follows: In Section 2, the standard k-ε model, realizable k-ε model, standard k–ω model, and SST k-ω model of computational fluid dynamics are described. Section 3 introduces the results of the influence of wind speed, wind direction, and turbulence model. Finally, Section 4 ends with some conclusions drawn from this study.

2. Computational Fluid Dynamics

Generally, the computational fluid dynamics of a bridge are calculated based on the finite element method [24–31]. For an incompressible fluid, the continuity equation and momentum equation can be expressed as [32]

$$\frac{\partial U_i}{\partial x_i} = 0 \tag{1}$$

$$\begin{gathered} U_j \frac{\partial U_i}{\partial x_j} = \frac{1}{\rho} \frac{\partial}{\partial x_j} (-P\delta_{ij} + 2\upsilon S_{ij} + \tau_{ij}) \\ S_{ij} = \frac{1}{2} \left(\frac{\partial U_i}{\partial x_j} + \frac{\partial U_j}{\partial x_i} \right) \end{gathered} \tag{2}$$

$$\tau_{ij} = \upsilon_t \left(\frac{\partial U_i}{\partial x_j} + \frac{\partial U_j}{\partial x_i} \right) - \frac{2}{3} k \delta_{ij} \tag{3}$$

where ρ is the density of air, $\rho = 1.293\ \mathrm{kg/m^3}$; υ is the kinematic viscosity, $\upsilon = 17.9 \times 10^{-6}\ \mathrm{m^2/s}$; P is the pressure, Pa; S_{ij} is the velocity strain rate tensor; δ_{ij} is the Kronecker delta; U_i are the mean velocity components, m/s; and k is the turbulent kinetic energy, $\mathrm{m^2/s^2}$.

Regarding the standard k-ε model, the transport equation of k can be expressed by [33]

$$\upsilon_t = C_\mu \frac{k^2}{\varepsilon} \tag{4}$$

$$\frac{\partial \rho k}{\partial t} + \frac{\partial \rho k U_i}{\partial x_i} = \frac{\partial}{\partial x_j} \left[\left(\upsilon + \frac{\upsilon_t}{\sigma_k} \right) \frac{\partial k}{\partial x_j} \right] + P_k - \rho\varepsilon \tag{5}$$

$$\frac{\partial \rho \varepsilon}{\partial t} + \frac{\partial \rho \varepsilon U_i}{\partial x_i} = \frac{\partial}{\partial x_j} \left[\left(\upsilon + \frac{\upsilon_t}{\sigma_\varepsilon} \right) \frac{\partial \varepsilon}{\partial x_j} \right] + \frac{\varepsilon}{k} (C_1 P_k - C_2 \rho\varepsilon) \tag{6}$$

where P_k is the production of turbulent kinetic energy, and $P_k = \upsilon_t S^2$, $S = \sqrt{2S_{ij}S_{ij}}$, and other constants are $C_\mu = 0.09$, $\sigma_\varepsilon = 1.3$, $\sigma_k = 1.0$, $C_1 = 1.44$, and $C_2 = 1.92$.

Regarding the realizable k-ε model, the transport equation of k can be expressed by [34]

$$\frac{\partial \rho \varepsilon}{\partial t} + \frac{\partial \rho \varepsilon U_i}{\partial x_i} = \frac{\partial}{\partial x_j} \left[\left(\upsilon + \frac{\upsilon_t}{\sigma_\varepsilon} \right) \frac{\partial \varepsilon}{\partial x_j} \right] + \rho C_{\varepsilon 1} S - \rho C_{\varepsilon 2} \frac{\varepsilon^2}{k + \sqrt{\varepsilon \upsilon}} \tag{7}$$

where $\overline{\Omega_{ij}}$ is the mean rate-of-rotation tensor viewed in a rotating reference frame with the angular velocity ω_k and the constants are $\sigma_\varepsilon = 1.2$, $C_{\varepsilon 2} = 1.9$, $C_{\varepsilon 1} = \max\left(0.43, \frac{k}{\varepsilon}\sqrt{2S_{ij}S_{ij}}\right)$, $C_\mu = \frac{1}{4.04 + \frac{A_s k U^*}{\varepsilon}}$, $A_s = \sqrt{6}\cos\theta$, $\theta = \frac{1}{3}\cos^{-1}\sqrt{6}W$, $S^* = \sqrt{S_{ij}S_{ij}}$, $U^* = \sqrt{S_{ij}S_{ij} + \Omega^*{}_{ij}\Omega^*{}_{ij}}$, $\Omega^*{}_{ij} = \Omega_{ij} - 2\varepsilon_{ijk}\omega_k$, and $\Omega_{ij} = \overline{\Omega_{ij}} - \varepsilon_{ijk}\omega_k$.

Regarding the standard k-ω model, the transport equations of k and ω are defined by [35]

$$v_{\omega t} = \frac{k}{\omega} \tag{8}$$

$$\frac{\partial k}{\partial t} + \frac{\partial k U_j}{\partial x_j} = \tau_{ij}\frac{\partial U_j}{\partial x_j} - \beta^* k\omega\rho + \frac{\partial}{\partial x_j}\left[(v + v_{\omega t}\sigma_{k1})\frac{\partial k}{\partial x_j}\right] \tag{9}$$

$$\frac{\partial \omega}{\partial t} + \frac{\partial \omega U_j}{\partial x_j} = \alpha\frac{\omega}{k}\tau_{ij}\frac{\partial U_j}{\partial x_j} - \beta_1\omega^2 + \frac{\partial}{\partial x_j}\left[(v + v_{\omega t}\sigma_{\omega 1})\frac{\partial \omega}{\partial x_j}\right] \tag{10}$$

where the constants are $\alpha = \frac{5}{9}$, $\beta_1 = 0.09$, $\sigma_{\omega 1} = 0.5$, and $\sigma_{k1} = 0.85$.

Regarding the SST k-ω model, the transport equations of k and ω are defined by [36,37]

$$v_{\omega t} = \frac{a_1 k}{\max(a_1\omega, F_2 S)} \tag{11}$$

$$\frac{\partial k}{\partial t} + \frac{\partial k U_j}{\partial x_j} = P_k - \beta^* k\omega + \frac{\partial}{\partial x_j}\left[(v + v_{\omega t}\sigma_{k2})\frac{\partial k}{\partial x_j}\right] \tag{12}$$

$$\frac{\partial \omega}{\partial t} + \frac{\partial \omega U_j}{\partial x_j} = \alpha S^2 - \beta_2\omega^2 + \frac{\partial}{\partial x_j}\left[(v + v_{\omega t}\sigma_{\omega 2})\frac{\partial \omega}{\partial x_j}\right] + 2(1 - F_1)\frac{\sigma_{\omega 2}}{\omega}\frac{\partial k}{\partial x_i}\frac{\partial \omega}{\partial x_i} \tag{13}$$

$$P_k = \min\left(\tau_{ij}\frac{\partial U_i}{\partial x_j}, 10\beta^* k\omega\right) \tag{14}$$

$$F_1 = \tanh\left\{\left[\min\left(\max\left(\frac{\sqrt{k}}{\beta^* y\omega}, \frac{500v}{y^2\omega}\right), \frac{4\sigma_{\omega 2}k}{CD_{k\omega}y^2}\right)\right]^4\right\} \tag{15}$$

$$F_2 = \tanh\left\{\left[\max\left(\frac{2\sqrt{k}}{\beta^* y\omega}, \frac{500v}{y^2\omega}\right)\right]^2\right\} \tag{16}$$

$$CD_{k\omega} = \max\left(2\rho\frac{\sigma_{\omega 2}}{\omega}\frac{\partial k}{\partial x_i}\frac{\partial \omega}{\partial x_i}, 10^{-10}\right) \tag{17}$$

where the constants are $\beta_2 = 0.0828$, $\sigma_{\omega 2} = 0.856$, $\sigma_{k2} = 1$, and $a_1 = 0.31$.

3. Calculation and Analysis

Figure 1 shows the investigated bridge. Regarding the investigated bridge hangers, their diameter is 0.077 m, their modulus of elasticity is 1.9×10^8 kpa, their bulk density is 7850 kN/m^3, and their Poisson's ratio is 0.3. Regarding the boundary conditions of the bridge hangers, they have a fixed constraint on the upper and lower.

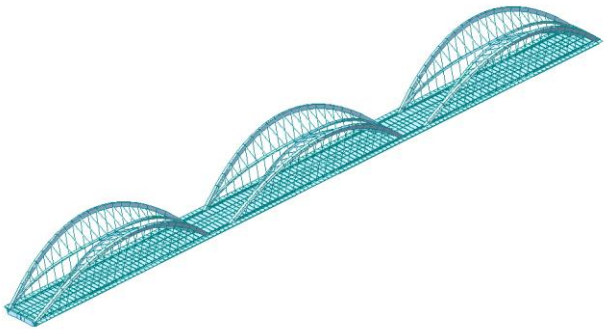

Figure 1. Investigated bridge.

COMSOL Multiphysics is a general finite element software that can be used to calculate fluid dynamics, solid mechanics, multifield coupling, and so forth [38]. Regarding the finite element model, the left boundary is the wind speed inlet, the right boundary is the outlet, and the upper and lower boundaries are slip boundaries, which are the same boundary conditions with a wind tunnel test. Regarding the bridge section, there are 9994 domain elements and 334 boundary elements, and the mesh is encrypted at the boundary. Regarding the finite element model, it has the four slip boundaries, the wind speed inlet, and the wind speed outlet, which can be seen in Figure 2a. Finally, the finite element model is divided into 35,377,709 units based on the finite volume method to solve the fluid governing equations, which can be seen in Figure 2b.

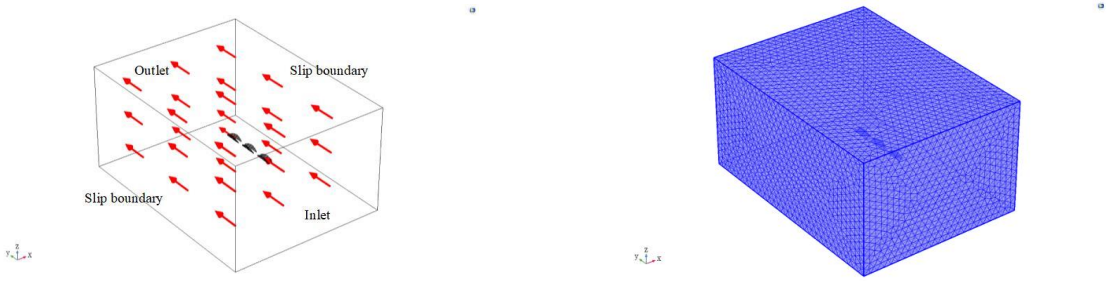

(**a**) Wind field simulation (**b**) Calculation mesh

Figure 2. Finite element model: (**a**) shows the boundary conditions of wind field simulation based on finite element model; (**b**) shows the calculation meshing in the wind field simulation based on the finite element model.

3.1. Influence of CFD Models

In this case study, the wind speed is 12 m/s and the wind direction is 90 degree. The changes in a bridge hanger's wind field at different CFD models are calculated, which can be seen as Figure 3. The calculation result of the SST *k*-*ω* model is different from that of the standard *k*-*ε* model, realizable *k*-*ε* model, and standard *k*-*ω* model, such as the wake flow characteristics of a hanger. Regarding the calculation result of the standard *k*-*ε* model, realizable *k*-*ε* model, and standard *k*-*ω* model, their wind field is the same. Therefore, the standard *k*-*ε* model is selected to calculate the turbulence equation.

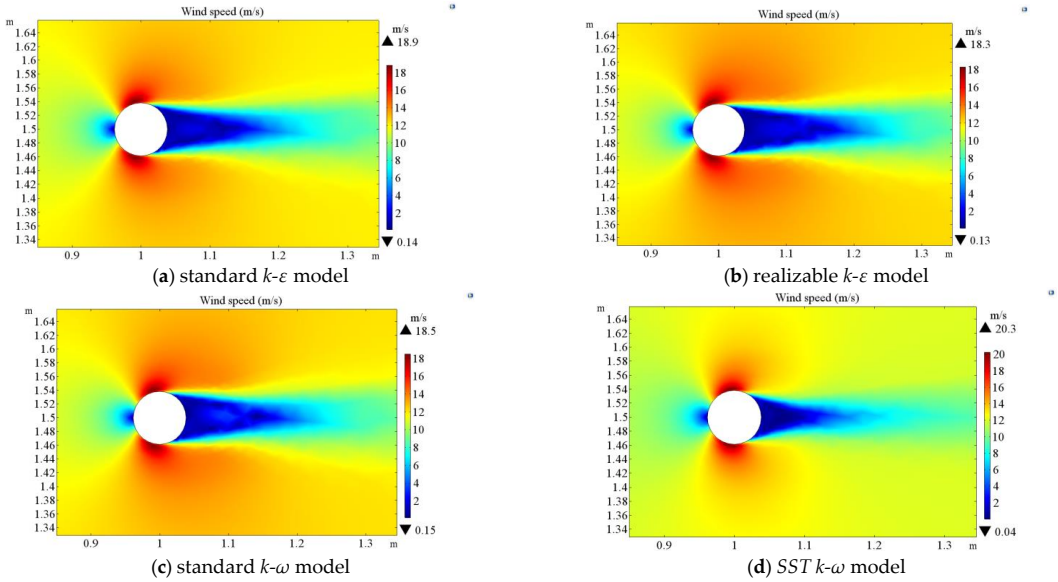

(**a**) standard *k*-*ε* model (**b**) realizable *k*-*ε* model

(**c**) standard *k*-*ω* model (**d**) *SST k*-*ω* model

Figure 3. Influence of CFD models on the wind field: (**a**) shows the wind speed variation under the standard *k*-*ε* model; (**b**) shows the wind speed variation under the realizable *k*-*ε* model; (**c**) shows the wind speed variation under the standard *k*-*ω* model; (**d**) shows the wind field speed under the SST *k*-*ω* model.

3.2. Influence of Wind Speed

In this case study, we assume the wind direction is 0 degree and the wind speed is adjustable. The changes in the bridge hangers' stress at different wind speeds are calculated based on the *k*–ε model and dynamic equations, which can be seen in Figure 4. When the wind speed increases from 3 to 12 m/s, the von Mises stress of the bridge hangers is nonlinearly increasing.

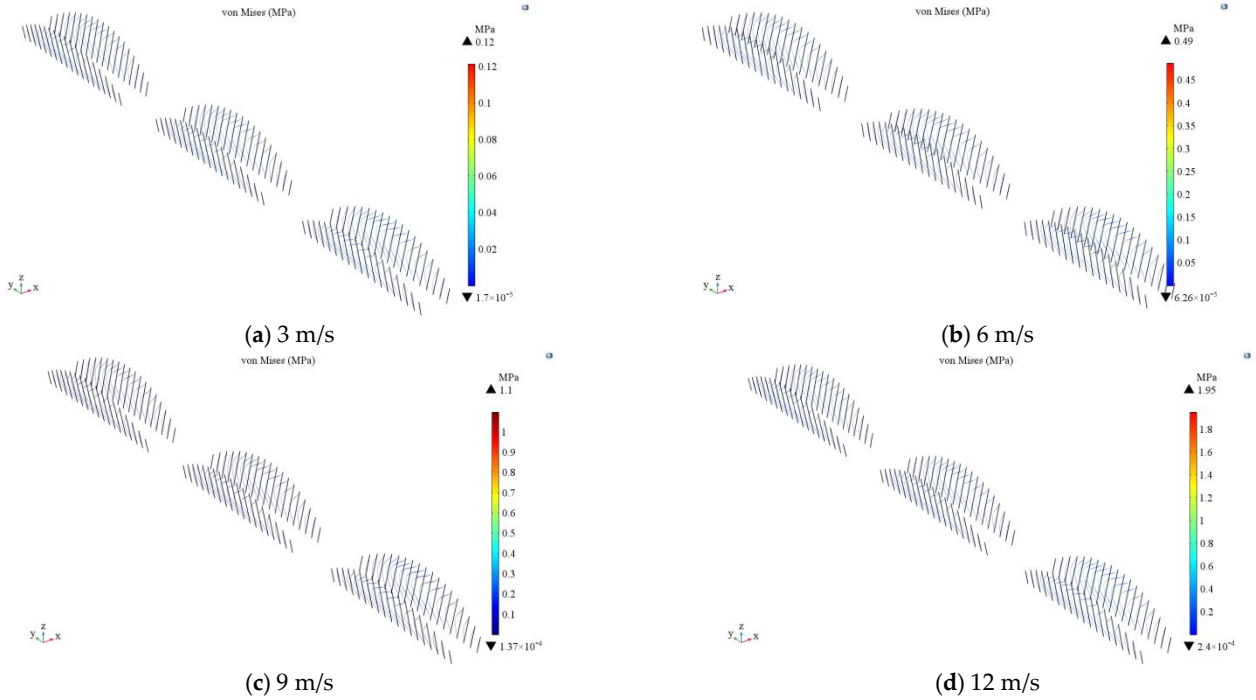

(**a**) 3 m/s (**b**) 6 m/s

(**c**) 9 m/s (**d**) 12 m/s

Figure 4. Influence of wind speed on stress: (**a**) shows the von Mises variation under the 3 m/s; (**b**) shows the von Mises variation under the 6 m/s; (**c**) shows the von Mises variation under the 9 m/s; (**d**) shows the von Mises variation under the 12 m/s.

3.3. Influence of Wind Direction

In this case study, the wind speed is 12 m/s and the wind direction is adjustable. The changes in the bridge hangers' wind field at different wind directions are calculated based on the *k*–ε model and dynamic equations, which can be seen in Figure 5. On the one hand, the wind field is different at different heights with the same wind speed. On the other hand, when the wind direction increases from 0 to 90 degrees, the wind speed field changes too.

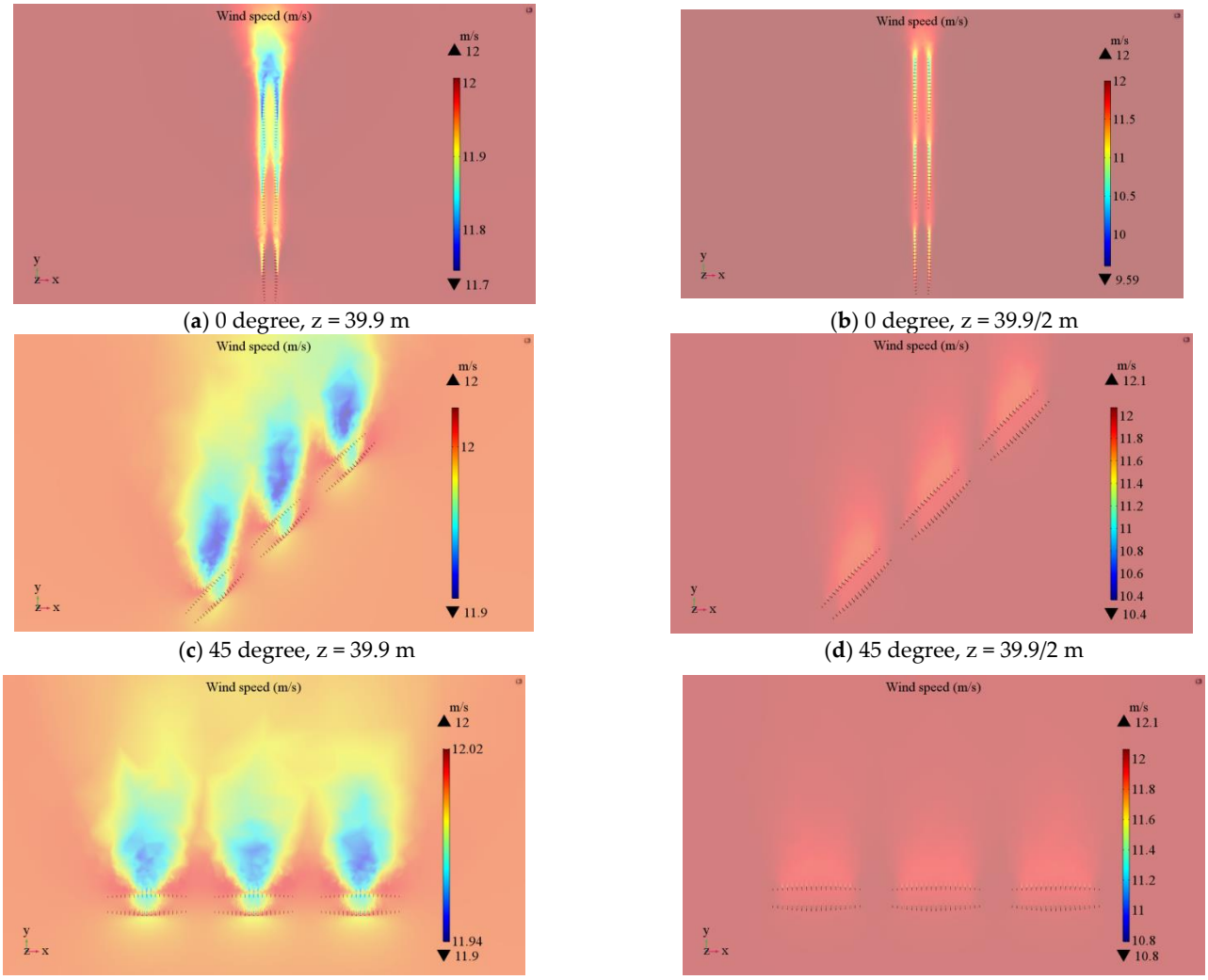

Figure 5. Influence of wind direction on wind field: (**a**) shows the wind speed variation under the 0 degree, z = 39.9 m; (**b**) shows the wind speed variation under the 0 degree, z = 39.9/2 m; (**c**) shows the wind speed variation under the 45 degree, z = 39.9 m; (**d**) shows the wind speed variation under the 45 degree, z = 39.9/2 m; (**e**) shows the wind speed variation under the 90 degree, z = 39.9 m; (**f**) shows the wind speed variation under the 90 degree, z = 39.9/2 m.

The changes in the bridge hangers' stress at different wind directions are calculated based on the k–ε model and dynamic equations, which can be seen in Figures 4d and 6.

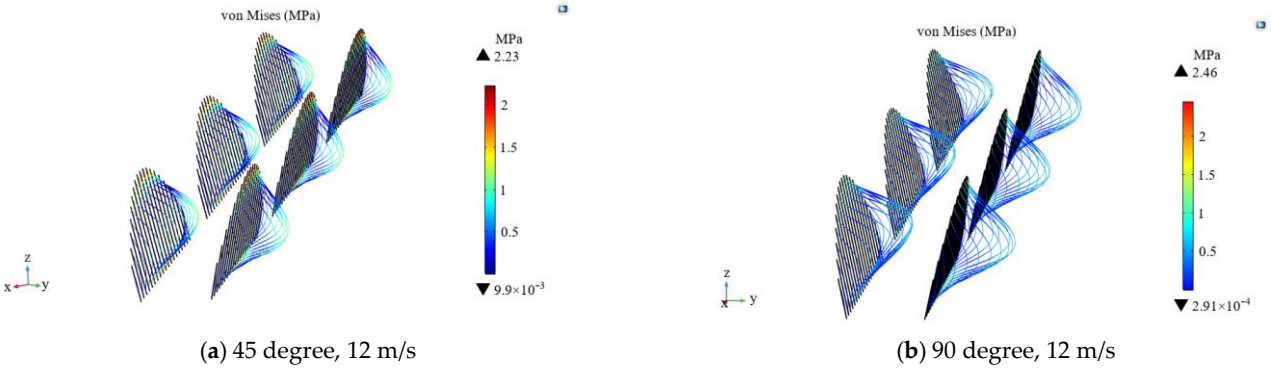

Figure 6. Influence of wind direction on stress: (**a**) shows the von Mises variation under the 45 degree, 12 m/s; (**b**) shows the von Mises variation under the 90 degree, 12 m/s.

4. Discussion and Conclusions

This case analyzes the finite element model of investigated bridge hangers through COMSOL Multiphysics software. The influences of CFD models, wind speed, and wind direction on the bridge hangers are investigated through case studies, and the von Mises stress of the bridge hangers is calculated based on fluid–solid coupling. The main conclusions drawn from this study are summarized as follows:

1. The calculation result of the SST k-ω model is different from that of the standard k-ε model, realizable k-ε model, and standard k-ω model, such as the wake flow characteristics of a hanger. Therefore, we will use the standard k-ε model to calculate the von Mises stress time history curve of bridge hangers and then assess the fatigue life of bridge hangers in a future work.
2. The larger is the wind speed, the larger is the effect on the wind field and stress for the investigated bridge hangers. For example, when the wind speed increases from 3 to 12 m/s, the stress of the bridge hangers nonlinearly increases. Therefore, the influence of the bridge hangers should be a concern under a strong wind speed during the operation.
3. Regarding the different wind directions with the same wind speed, the influence of the bridge hangers is also different. For example, when the wind direction increases from 0 to 90 degrees, the fatigue life of the bridge hangers decreases. Therefore, the influence of wind direction on the investigated bridge hangers cannot be ignored.

Author Contributions: Funding acquisition, J.-L.D. and S.-X.Z.; investigation, Y.D.; methodology, Y.D.; software, Y.D.; supervision, T.-L.Y.; writing—review and editing, Y.D., S.-X.Z. and Y.-Q.W. All authors have read and agreed to the published version of the manuscript.

Funding: This work was supported by a Key R&D Project of National (grant nos. 2019 YFC1906203, 2017YFC0504506, 2017YFC0504503, and 2016YFC0700807), a Key R&D Project of Jiangxi Province (grant no. 20171BBG70078), the Natural Science Foundation of China (grant nos. 52163034, 51108341, 51662008, 51968022, and 51708220), and an Opening Project of Key Laboratory of Soil and Water Loss Process and Control in Loess Plateau, Ministry of Water Resources (grant no. 201806).

Institutional Review Board Statement: Ethical review and approval were waived for this study because the institutions of the authors who participated in the data collection do not require IRB review and approval.

Informed Consent Statement: Not applicable.

Data Availability Statement: Data are contained within the article.

Conflicts of Interest: The authors declare no conflict of interest.

References

1. Xu, S.Q.; Ma, R.J.; Wang, D.; Chen, A.; Tian, H. Prediction analysis of vortex-induced vibration of long-span suspension bridge based on monitoring data. *J. Wind Eng. Ind. Aerodyn.* **2019**, *191*, 312–324. [CrossRef]
2. Shum, K.M.; Xu, Y.L.; Guo, W.H. Wind-induced vibration control of long span cable-stayed bridges using multiple pressurized tuned liquid column dampers. *J. Wind Eng. Ind. Aerodyn.* **2008**, *96*, 166–192. [CrossRef]
3. Li, S.; Laima, S.; Li, H. Data-driven modeling of vortex-induced vibration of a long-span suspension bridge using decision tree learning and support vector regression. *J. Wind Eng. Ind. Aerodyn.* **2018**, *172*, 196–211. [CrossRef]
4. Li, S.L.; An, Y.H.; Wang, C.Q.; Wang, D.W. Experimental and numerical studies on galloping of the flat-topped main cables for the long span suspension bridge during construction. *J. Wind Eng. Ind. Aerodyn.* **2017**, *163*, 24–32. [CrossRef]
5. Casalotti, A.; Arena, A.; Lacarbonara, W. Mitigation of post-flutter oscillations in suspension bridges by hysteretic tuned mass dampers. *Eng. Struct.* **2014**, *69*, 62–71. [CrossRef]
6. Ding, Y.; Dong, J.; Yang, T.; Zhou, S.; Wei, Y. Failure Evaluation of Bridge Deck Based on Parallel Connection Bayesian Network: Analytical Model. *Materials* **2021**, *14*, 1411. [CrossRef] [PubMed]
7. Ni, Y.Q.; Xia, Y.; Liao, W.Y.; Ko, J.M. Technology innovation in developing the structural health monitoring system for guangzhou new tv tower. *Struct. Control Health Monit.* **2009**, *16*, 73–98. [CrossRef]
8. Lin, L.; Chen, K.; Xia, D.; Wang, H.; Hu, H.; He, F. Analysis on the wind characteristics under typhoon climate at the southeast coast of china. *J. Wind Eng. Ind. Aerodyn.* **2018**, *182*, 37–48. [CrossRef]

9. Wang, H.; Li, A.; Niu, J.; Zong, Z.; Li, J. Long-term monitoring of wind characteristics at sutong bridge site. *J. Wind Eng. Ind. Aerodyn.* **2013**, *115*, 39–47. [CrossRef]
10. Xu, Y.L. Making good use of structural health monitoring systems of long-span cable-supported bridges. *J. Civ. Struct. Health Monit.* **2018**, *8*, 477–497. [CrossRef]
11. Koo, K.Y.; Brownjohn, J.M.W.; List, D.I.; Cole, R. Structural health monitoring of the Tamar suspension bridge. *Struct. Control Health Monit.* **2013**, *20*, 609–625. [CrossRef]
12. Ding, Y.; Zhou, G.; Li, A.; Deng, Y. Statistical characteristics of sustained wind environment for a long-span bridge based on long-term field measurement data. *Wind Struct.* **2013**, *17*, 43–68. [CrossRef]
13. Saha, U.K.; Thotla, S.; Maity, D. Optimum design configuration of savonius rotor through wind tunnel experiments. *J. Wind Eng. Ind. Aerodyn.* **2008**, *96*, 1359–1375. [CrossRef]
14. Zajaczkowski, F.J.; Haupt, S.E.; Schmehl, K.J.; Jweia, J.; Model, W.F. A preliminary study of assimilating numerical weather prediction data into computational fluid dynamics models for wind prediction. *J. Wind Eng. Ind. Aerodyn.* **2011**, *99*, 320–329. [CrossRef]
15. Jeong, W.M.; Liu, S.N.; Jakobsen, J.B.; Ong, M.C. Unsteady RANS simulations of flow around a twin-box bridge girder cross section. *Energies* **2019**, *12*, 2670. [CrossRef]
16. Matsumoto, M.; Shijo, R.; Eguchi, A.; Hikida, T.; Mizuno, K. On the flutter characteristics of separated two box girders. *Wind Struct. Int. J.* **2004**, *7*, 281–291. [CrossRef]
17. Hu, C.; Zhou, Z.; Jiang, B. Effects of types of bridge decks on competitive relationships between aerostatic and flutter stability for a super long cable-stayed bridge. *Wind Struct.* **2019**, *28*, 255–270.
18. Zhu, L.D.; Li, L.; Xu, Y.L.; Zhu, Q. Wind tunnel investigations of aerodynamic coefficients of road vehicles on bridge deck. *J. Fluids Struct.* **2012**, *30*, 35–50. [CrossRef]
19. Montoya, M.C.; Nieto, F.; Hernández, S.; Kusano, I.; Jurado, J.Á. Cfd-based aeroelastic characterization of streamlined bridge deck cross-sections subject to shape modifications using surrogate models. *J. Wind Eng. Ind. Aerodyn.* **2018**, *177*, 405–428. [CrossRef]
20. Thordal, M.S.; Bennetsen, J.C.; Koss, H.H.H. Review for practical application of cfd for the determination of wind load on high-rise buildings. *J. Wind Eng. Ind. Aerodyn.* **2019**, *186*, 155–168. [CrossRef]
21. Scappaticci, L.; Castellani, F.; Astolfi, D.; Garinei, A. Diagnosis of vortex induced vibration of a gravity damper. *Diagnostyka* **2018**, *19*, 31–39. [CrossRef]
22. Huang, W.; Yang, Q.; Hong, X. Cfd modeling of scale effects on turbulence flow and scour around bridge piers. *Comput. Fluids* **2009**, *38*, 1050–1058. [CrossRef]
23. Shirai, S.; Ueda, T. Aerodynamic simulation by cfd on flat box girder of super-long-span suspension bridge. *J. Wind Eng. Ind. Aerodyn.* **2003**, *91*, 279–290. [CrossRef]
24. Khalilzadeh, A.; Ge, H.; Ng, H.D. Effect of turbulence modeling schemes on wind-driven rain deposition on a mid-rise building: Cfd modeling and validation. *J. Wind Eng. Ind. Aerodyn.* **2019**, *184*, 362–377. [CrossRef]
25. Haque, S.M.E.; Rasul, M.G.; Khan, M.M.K.; Deev, A.V.; Subaschandar, N. Influence of the inlet velocity profiles on the prediction of velocity distribution inside an electrostatic precipitator. *Exp. Therm. Fluid Sci.* **2009**, *33*, 322–328. [CrossRef]
26. Sun, D.; Owen, J.S.; Wright, N.G. Application of the k–ω turbulence model for a wind-induced vibration study of 2d bluff bodies. *J. Wind Eng. Ind. Aerodyn.* **2009**, *97*, 77–87. [CrossRef]
27. Xu, G.; Cai, C.S. Numerical investigation of the lateral restraining stiffness effect on the bridge deck-wave interaction under stokes waves. *Eng. Struct.* **2017**, *130*, 112–123. [CrossRef]
28. De, M.S.; Patruno, L.; Ubertini, F.; Vairo, G. Indicial functions and flutter derivatives: A generalized approach to the motion-related wind loads. *J. Fluids Struct.* **2013**, *42*, 466–487.
29. Glück, M.; Breuer, M.; Durst, F.; Halfmann, A.; Rank, E. Computation of wind-induced vibrations of flexible shells and membranous structures. *J. Fluids Struct.* **2003**, *17*, 739–765. [CrossRef]
30. Santo, G.; Peeters, M.; Van Paepegem, W.; Degroote, J. Dynamic load and stress analysis of a large horizontal axis wind turbine using full scale fluid-structure interaction simulation. *Renew. Energy* **2019**, *140*, 212–226. [CrossRef]
31. Wu, Y.L.; Qi, L.J.; Zhang, H.; Musiu, E.; Yang, Z.P.; Wang, P. Design of UAV downwash airflow field detection system based on strain effect principle. *Sensors* **2019**, *19*, 2630. [CrossRef]
32. Qi, Y.H.; Ishihara, T. Numerical study of turbulent flow fields around of a row of trees and an isolated building by using modified k-ε model and les model. *J. Wind Eng. Ind. Aerodyn.* **2018**, *177*, 293–305. [CrossRef]
33. Nakajima, K.; Ooka, R.; Kikumoto, H. Evaluation of k-ε reynolds stress modeling in an idealized urban canyon using les. *J. Wind Eng. Ind. Aerodyn.* **2018**, *175*, 213–228. [CrossRef]
34. Lateb, M.; Masson, C.; Stathopoulos, T.; Bédard, C. Comparison of various types of k–ε models for pollutant emissions around a two-building configuration. *J. Wind Eng. Ind. Aerodyn.* **2013**, *115*, 9–21. [CrossRef]
35. Wilcox, D.C. Reassessment of the scale-determining equation for advanced turbulence models. *AIAA J.* **1988**, *26*, 1299–1310. [CrossRef]
36. Menter, F.R. Two-equation eddy-viscosity turbulence models for engineering applications. *AIAA J.* **1994**, *32*, 1598–1605. [CrossRef]
37. Menter, F.R. Zonal two equation k-ω turbulence models for aerodynamic flows. *AIAA J.* **1993**, *6*, 2893–2906.
38. Ding, Y.; Yang, T.L.; Liu, H.; Han, Z.; Zhou, S.X.; Wang, Z.P.; She, A.M.; Wei, Y.-Q.; Dong, J.L. Experimental study and simulation calculation of the chloride resistance of concrete under multiple factors. *Appl. Sci.* **2021**, *11*, 5322. [CrossRef]